



Article

Global Evaluation and Intercomparison of XCO₂ Retrievals from GOSAT, OCO-2, and TANSAT with TCCON

Junjun Fang^{1,2}, Baozhang Chen^{1,2,3} , Huifang Zhang^{1,2,*}, Adil Dilawar^{1,2,4} , Man Guo^{1,5} , Chunlin Liu³, Shu'an Liu³, Tewekel Melese Gemechu^{1,2} and Xingying Zhang⁶

¹ State Key Laboratory of Resources and Environmental Information System, Institute of Geographic Sciences and Natural Resources Research, Chinese Academy of Sciences, Beijing 100101, China; fangjunjun21@mails.ucas.ac.cn (J.F.); baozhang.chen@igsrr.ac.cn (B.C.); adilawar2018@igsrr.ac.cn (A.D.); sgxmg1@nottingham.edu.cn (M.G.); tmgemechu2022@igsrr.ac.cn (T.M.G.)

² University of Chinese Academy of Sciences, Beijing 100049, China

³ School of Remote Sensing and Geomatics Engineering, Nanjing University of Information Science and Technology, Nanjing 210044, China; 20201248055@nuist.edu.cn (C.L.); 20201111005@nuist.edu.cn (S.L.)

⁴ State Key Laboratory of Earth Surface and Ecological Resources, Faculty of Geographical Science, Beijing Normal University, Beijing 100875, China

⁵ School of Geographical Sciences, Faculty of Science and Engineering, University of Nottingham, Ningbo 315100, China

⁶ National Satellite Meteorological Center, China Meteorological Administration, Beijing 100081, China; zxy@cma.gov.cn

* Correspondence: zhanghf@reis.ac.cn; Tel.: +86-010-6488-9574

Abstract: Accurate global monitoring of carbon dioxide (CO₂) is essential for understanding climate change and informing policy decisions. This study compares column-averaged dry-air mole fractions of CO₂ (XCO₂) between ACOS_L2_Lite_FP V9r for Japan's Greenhouse Gases Observing Satellite (GOSAT), OCO-2_L2_Lite_FP V10r for the USA's Orbiting Carbon Observatory-2 (OCO-2), and IAPCAS V2.0 for China's Carbon Dioxide Observation Satellite (TANSAT) collectively referred to as GOT, with data from the Total Carbon Column Observing Network (TCCON). Our findings are as follows: (1) Significant data quantity differences exist between OCO-2 and the other satellites, with OCO-2 boasting a data volume 100 times greater. GOT shows the highest data volume between 30–45°N and 20–30°S, but data availability is notably lower near the equator. (2) XCO₂ from GOT exhibits similar seasonal variations, with lower concentrations during June, July, and August (JJA) (402.72–403.74 ppm) and higher concentrations during December, January, and February (DJF) (405.74–407.14 ppm). XCO₂ levels are higher in the Northern Hemisphere during March, April, and May (MAM) and DJF, while slightly lower during JJA and September, October, and November (SON). (3) The differences in XCO₂ (Δ XCO₂) reveal that Δ XCO₂ between OCO-2 and TANSAT are minor (-0.47 ± 0.28 ppm), whereas the most significant difference is observed between GOSAT and TANSAT (-1.13 ± 0.15 ppm). Minimal differences are seen in SON (with the biggest difference between GOSAT and TANSAT: -0.84 ± 0.12 ppm), while notable differences occur in DJF (with the biggest difference between GOSAT and TANSAT: -1.43 ± 0.17 ppm). Regarding latitudinal variations, distinctions between OCO-2 and TANSAT are most pronounced in JJA and SON. (4) Compared to TCCON, XCO₂ from GOT exhibits relatively high determination coefficients ($R^2 > 0.8$), with GOSAT having the highest root mean square error (RMSE = 1.226 ppm, <1.5 ppm), indicating a strong relationship between ground-based observed and retrieved values. This research contributes significantly to our understanding of the spatial characteristics of global XCO₂. Furthermore, it offers insights that can inform the analysis of differences in the inversion of carbon sources and sinks within assimilation systems when incorporating XCO₂ data from satellite observations.

Keywords: carbon satellites; XCO₂; TCCON; cross-validation; remote sensing



Citation: Fang, J.; Chen, B.; Zhang, H.; Dilawar, A.; Guo, M.; Liu, C.; Liu, S.; Gemechu, T.M.; Zhang, X. Global Evaluation and Intercomparison of XCO₂ Retrievals from GOSAT, OCO-2, and TANSAT with TCCON. *Remote Sens.* **2023**, *15*, 5073. <https://doi.org/10.3390/rs15205073>

Academic Editor: Beatriz M. Funatsu

Received: 7 September 2023

Revised: 11 October 2023

Accepted: 20 October 2023

Published: 23 October 2023



Copyright: © 2023 by the authors. Licensee MDPI, Basel, Switzerland. This article is an open access article distributed under the terms and conditions of the Creative Commons Attribution (CC BY) license (<https://creativecommons.org/licenses/by/4.0/>).

1. Introduction

The Earth's climate system is experiencing profound changes, primarily due to anthropogenic activities, with the emission of greenhouse gases (GHGs) into the atmosphere [1–3]. Among these GHGs, carbon dioxide (CO₂) has the utmost importance due to its long-lasting effects and pivotal role in driving global warming [4,5]. The accurate measurement and monitoring of atmospheric CO₂ concentrations are crucial for assessing the rate of climate change, understanding its impacts on ecosystems, and formulating effective mitigation strategies [6,7].

Traditional ground-based measurements, while providing valuable data, have limitations in terms of spatial coverage and the comprehensive capture of intricate nuances in atmospheric CO₂ distribution patterns. This limitation has prompted the development of carbon satellite-based missions in different countries. For example, Japan's Greenhouse Gases Observing Satellite (GOSAT) [8], the Orbiting Carbon Observatory-2 (OCO-2) mission operated by the National Aeronautics and Space Administration (NASA) [9,10], and China's Carbon Dioxide Observation Satellite Mission (TANSAT) [11,12], collectively referred to as GOT, provide globally averaged dry-air mole fractions of CO₂ (XCO₂) at various temporal and spatial scales.

In the realm of satellite-based CO₂ measurements, significant advancements have been achieved in XCO₂ retrieval algorithms, atmospheric correction methods, and validation techniques [13–17]. Many studies have utilized GOSAT and OCO-2 data to investigate CO₂ concentration distributions at both regional and global scales [18–21]. Furthermore, in anticipation of future decision-making regarding emission reduction strategies and climate change mitigation, there is a pressing need for highly precise information regarding CO₂ sources and sinks. In response to this urgency, numerous researchers have endeavored to assess the dynamic interplay of carbon sources and sinks in terrestrial ecosystems by leveraging GOSAT and OCO-2 satellite data along with diverse inversion methods [22–25]. These studies have made significant contributions to unraveling the complexities of CO₂ sources and sinks, as well as the integral role of landmasses, oceans, and vegetation in the intricate carbon cycle [25–29].

However, despite these advancements, challenges and controversies persist in accurately quantifying the temporal and spatial variability of CO₂ sources and sinks for various reasons [28,30,31]. These reasons include: (1) inherent limitations in atmospheric CO₂ observations [32]; (2) the capabilities of model simulations [33]; and (3) data uncertainties in observational conditions. In this context, our focus is on the third point. Although carbon satellites help mitigate some of the limitations of sparse data, existing satellite missions emphasize that cloud-free observations are captured on less than 2% of the Earth's surface area, even on a monthly basis [34]. Previous studies have also highlighted the significant influence of model setup in perpetuating uncertainty in carbon budgets and China's terrestrial ecosystems. This study underscores the need for a larger ensemble of inversion systems to address this challenge [32]. Integrating XCO₂ data derived from carbon satellites into inversion models to retrieve carbon source and sink information presents another challenge. Discrepancies between satellite data and ground measurements, such as those obtained from the Total Carbon Column Observing Network (TCCON), have been reported [15,35–39]. These disparities can be attributed to various factors, including instrumental biases, uncertainties in atmospheric corrections, and differences in spatiotemporal resolutions. Understanding these discrepancies is crucial for further improving the quality of satellite-based CO₂ measurements and enhancing our comprehension of datasets when integrated into inversion models.

Despite the extensive comparisons conducted among various carbon satellite datasets and their respective correlations with TCCON data, there is a noticeable gap in comprehensive studies that simultaneously compare data from GOSAT, OCO-2, and TANSAT. In the case of China, specifically, understanding the differences between XCO₂ data from domestic satellites and international XCO₂ data is essential for setting satellite parameters

and improving data quality. This understanding will help us better achieve our goals of carbon peak and carbon neutrality.

In our study, we aim to conduct a comprehensive comparative analysis of XCO₂ data from GOT (referred to as XGOT) to assess the consistency and discrepancies within their XCO₂ measurements, covering several critical aspects. We will scrutinize factors such as the satellite's orbital characteristics and sensor parameters, as well as perform an intercomparison of XGOT data from seasonal, spatial, and latitudinal perspectives. Additionally, our investigation will involve discerning the contrasts between XGOT data and the data obtained from TCCON. Examining the similarities and discrepancies between the datasets from these missions will make a significant contribution to addressing existing issues. Our efforts are geared towards shedding light on the reliability and inherent limitations of satellite-based XCO₂ observations. Furthermore, we will use these XGOT data to invert the carbon source and sink using a carbon tracking model (CT-China) [40] in the near future, exploring how disparities in XCO₂ data influence the results of assimilation inversions. The findings from this study hold the potential to provide strong support for our subsequent, in-depth investigation into disparities among the three satellite-derived carbon sink inversions. This endeavor also serves as a valuable comparative case study for the research community utilizing these three distinct XCO₂ datasets.

We have structured this paper as follows: In Section 2, we describe the data, including XCO₂ from GOT and TCCON observations, and the methods we use to intercompare three satellite XCO₂ datasets and evaluate the differences between satellite XCO₂ and TCCON. Section 3 presents the results of the intercomparison and difference evaluation between satellite XCO₂ and TCCON. In Section 4, we discuss the uncertainties and implications of the results and draw conclusions.

2. Materials and Methods

2.1. Datasats

Our research datasets included XCO₂ data retrieved from GOT and ground validation sites (TCCON). Table 1 displays the orbit and observation geometry parameters as well as spectral information for each satellite sensor.

Table 1. Orbits, observation geometry, and sensor parameters of GOSAT, OCO-2, and TANSAT.

Satellites' Characteristics	GOSAT [8]	OCO-2 [41]	TANSAT [42]
Launch time	2009.01	2014.07	2016.12
Orbit Height/km	666	705	712
Inclination (°)	98.1	98.2	98.2
Recurrent Period/day	3	16	16
Local Time	12:45–12:55	13:30 ± 0.15	13:30
Pointing	Multiple targets with a 2-axis pointing mechanism	Nadir, Glint, Target	Nadir, Glint, Target
Swath/km	790	10.6	18
Footprint (Nadir)	Circle of 10.5 km diameter	1.29 × 2.25 km ²	2 × 2 km ²
Sensors	FTS, CAI	3-Channel Grating Spectrometer	ACGS, CAPI
Bands/μm	0.76–0.78, 1.56–1.72, 1.92–2.08, 5.56–14.30	0.76–0.77, 1.59–1.62, 2.04–2.08	0.76–0.77, 1.59–1.62, 2.04–2.08

2.1.1. Greenhouse Gases Observing Satellite (GOSAT)

GOSAT, Japan's first high-spectral resolution satellite, was launched in 2009 to observe GHGs in the atmosphere. It orbits along a solar quasi-return trajectory at an average altitude of 666 km and an inclination of 98.1°. Its revisit period is 3 days, with the descending node transiting between approximately 12:45 p.m. and 12:55 p.m. local time [43]. The satellite's carbon observation instrument, TANSO, consists of two sensors: the Fourier Transform Spectrometer (FTS) and the Cloud and Aerosol Imager (CAI). The FTS detects

GHG signals, while the CAI collects synchronized cloud and aerosol information. Specifically, the FTS wavelength band of 1.56–1.72 μm is used for inverting atmospheric XCO₂ [44]. Its instantaneous field of view (IFOV) spans 15.8 mrad, corresponding to a diameter range of approximately 10.5 km at the lower point of nadir observation. The satellite's scanning angle encompasses $\pm 20^\circ$ in the orbital direction and $\pm 35^\circ$ in the side-scanning direction [8].

The XCO₂ data used in this study were obtained from the ACOS_L2_Lite_FP product (V9r) [22]. The inversion algorithm employed is the ACOS algorithm [8], which is detailed in the ACOS Algorithm Level 2 Standard Product and Lite Data Product User's Guide [45]. The accuracy of the concentration observations is approximately 1 ppm. The data were archived at the Goddard Earth Science Data Information and Services Center (GES DIS) [46]. For this study, we selected the time range from 1 March 2017 to 28 February 2018 (one year for seasonal analysis), based on the availability of data from GOT (XCO₂ data from TANSAT are only available after 1 March 2017). Data quality screening was performed here (using the algorithm developers' quality flag) to ensure subsequent analysis.

2.1.2. Orbiting Carbon Observatory-2 (OCO-2)

OCO-2, launched on 2 July 2014, represents NASA's pioneering mission aimed at monitoring atmospheric CO₂ levels. OCO-2 follows a near-polar, sun-synchronous orbit with an altitude of 705 km, an inclination of 98.2°, and a revisit period of 16 days [9]. Its orbital path intersects the local time at approximately 1:30 p.m. Equipped with a three-band grating hyperspectral spectrometer, OCO-2 facilitates precise measurements of CO₂ concentrations, crucial for scientific insights. The spectrometer covers the oxygen A band (0.758–0.773 μm), a weak CO₂ absorption band (1.591–1.621 μm), and a strong CO₂ absorption band (2.043–2.083 μm). These distinct spectral bands enable researchers to accurately discern variations in CO₂ concentrations [47].

OCO-2 operates in three observation modes: nadir, glint, and target mode. The nadir mode is employed when the zenith angle is less than 85°, thereby enhancing spatial resolution, mitigating cloud interference, and capturing valuable cloud-free samples. The glint mode focuses on improving the signal-to-noise ratio (SNR) by observing solar altitude angles below 75°, particularly enhancing observations over oceanic regions [48]. In proximity to ground-based validation sites, the target mode becomes operational, facilitating targeted observations lasting up to 9 min and providing approximately 12,000 observations within the designated location. In the context of nadir observations, OCO-2 employs a cross-track IFOV of 0.1° and an integration time of 0.333 s. This specific configuration results in 4 to 8 bypass footprints, each effectively covering an area of 1.29 km \times 2.25 km [49].

This study utilizes XCO₂ data from the OCO-2_L2_Lite_FP product (V10r), and the inversion algorithm employed is ACOS [47,50]. The resulting full-column estimates of XCO₂ have single-sounding precisions of approximately 0.5 ppm [51]. All data relevant to the current study are archived at the Goddard Earth Science Data Information and Services Center [46]. The XCO₂ data underwent screening adhering to quality markers (using the algorithm developers' quality flag) for subsequent utilization.

2.1.3. China's Carbon Dioxide Observation Satellite (TANSAT)

In 2016, China successfully launched its inaugural GHG observation satellite, TANSAT. It operates in a sun-synchronous orbit positioned at an altitude of 712 km with an inclination of 98.2°. The local time of its ascending node is 1:30 p.m., and it completes a full revisit cycle every 16 days [42]. TANSAT features two distinct instruments: the Hyperspectral Greenhouse Gas Sounder (ACGS) and the Cloud and Aerosol Polarization Imager (CAPI). The ACGS module specifically captures absorption bands of O₂ at 0.76 μm and CO₂ at 1.61 μm and 2.06 μm . The CAPI instrument, serving as a wide-angle and medium-resolution imaging spectrometer, provides supplementary information to address observational errors caused by clouds and aerosols [52]. TANSAT's observing modes primarily include nadir, glint, and target modes. In the nadir mode, the footprint measures 2 km \times 2 km, and each swath includes 9 such footprints [53]. The IFOV width spans 18 km. The data we used are

from version 2.0, level L1B, and the inversion algorithm used is the Institute of Atmospheric Physics Carbon dioxide retrieval Algorithm for Satellite remote sensing (IAPCAS) [54]. This algorithm achieves an impressive inversion accuracy of 1% (4 ppm) [52].

2.1.4. Total Carbon Column Observing Network (TCCON)

We utilized TCCON for assessing XCO₂ retrieved by GOT. TCCON operates ground-based Fourier transform spectrometers, capturing solar near-infrared spectra to retrieve XCO₂ values [55]. This method precisely aligns the instrument with solar radiation, reducing the influence of factors such as aerosols and thin clouds on the optical path. Moreover, TCCON is tied to WHO by an extensive aircraft intercomparison campaign, and as a result an air-mass-dependent and independent correction factor is applied to the network data. All of the above results in the collection of high-precision XCO₂ data [56]. The use of the same instruments and data processing methods ensures consistency across measurement sites, creating a unified dataset.

To establish a correspondence between GOT data and TCCON data, we accessed the GGG2020 and GGG2014 versions (available for download at <https://TCCONdata.org/>, accessed on 8 July 2023). The GGG2020 version comprises data from 31 distinct sites, while the GGG2014 version includes data from 35 sites. The 2020 version takes precedence, with supplementation from the 2014 version (see Figure 1 for more detail). In preparation for this dataset, a 3-sigma screening method (details of which can be found in the Methods section) was implemented before its use in our study.

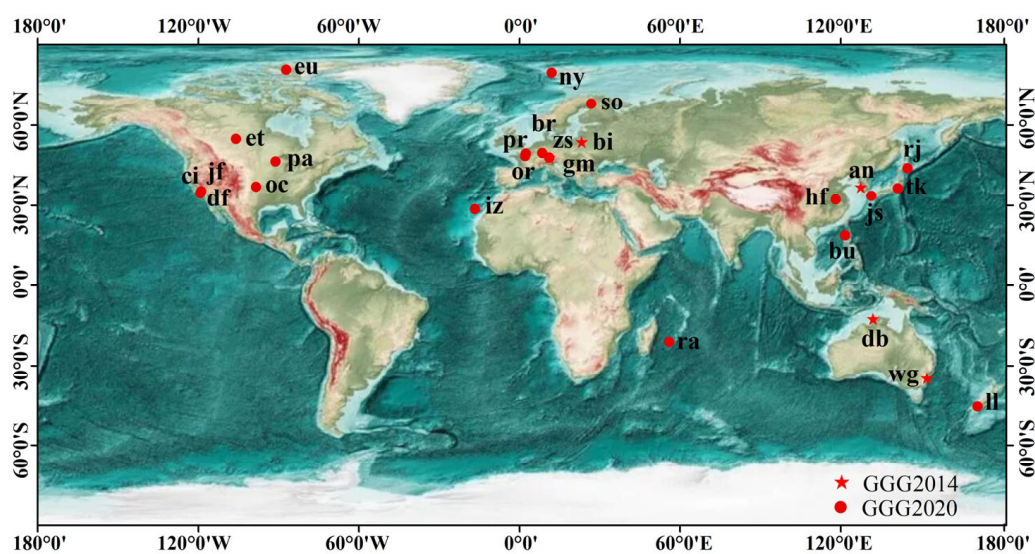


Figure 1. The spatial distribution of TCCON sites used in our study. See Table 2 for the full name of each site.

Since the XCO₂ dataset from three satellites covers the time range from March 2017 to February 2018, we conducted time matching with TCCON. The sites used by each satellite are listed in Table 2. The spatial distribution of all the sites used is illustrated in Figure 1.

We are aware that, for the land portion, the typical pointing mode for these three satellites is nadir, while for the ocean portion, it is usually the glint mode. To eliminate the difference between these two pointing modes, this study exclusively focused on the analysis of terrestrial areas.

2.2. Methods

2.2.1. Data Screening Method for TCCON

In our study, we employed a 3-sigma method to screen the TCCON data. Specifically, we selected data within the time range from March 2017 to February 2018 (to match the XGOT data) and calculated the differences between adjacent observations. We obtained

the average value (m) and standard deviation (σ) of these differences. Observations with differences that fell outside the range of $m \pm 3\sigma$ (forward and backward simultaneously) were considered outliers and were subsequently removed. To illustrate this process, we use the Burgos (bu) site as an example to demonstrate the contrast before and after the removal of abnormal values (Figure 2). The $m \pm \sigma$ changes from 406.629 ± 1.581 ppm to 406.632 ± 1.526 ppm after the removal of outliers, with the total number of observations going from 36,163 to 36,043 (0.3% of the data was excluded).

Table 2. TCCON site information used in our study and the number of pairs matched with satellites.

Sites Name	Abb	Locating (Long, Lat)	NC with GOSAT	NC with OCO-2	NC with TANSAT	Reference
Anmyeondo	an	126.33°E, 36.54°N	4	-	-	[57]
Bialystok	bi	23.02°E, 53.23°N	8	2	-	[58]
Burgos	bu	120.65°E, 18.53°N	6	9	-	[59]
Caltech	ci	118.13°W, 34.14°N	102	8	2	[60]
Darwin	db	130.89°E, 12.43°S	43	4	10	[61]
Dryden	df	117.88°W, 34.96°N	48	3	-	[62]
East Trout Lake	et	104.99°W, 54.36°N	-	8	4	[63]
Eureka	eu	86.42°W, 80.05°N	-	2	-	[64]
Garmisch	gm	11.06°E, 47.48°N	8	2	-	[65]
Hefei	hf	117.17°E, 31.9°N	2	-	2	[66]
Izana	iz	16.5°W, 28.31°N	-	2	-	[67]
PL, Pasadena	jf	118.18°W, 34.2°N	198	17	2	[68]
Saga	js	130.29°E, 33.24°N	33	8	-	[69]
Karlsruhe	ka	8.44°E, 49.1°N	6	12	-	[70]
Lauder	ll	169.68°E, 45.04°S	42	12	5	[71]
Ny-Ålesund	ny	11.92°E, 78.92°N	-	-	2	[72]
Lamont	oc	97.49°W, 36.6°N	59	31	10	[73]
Orléans	or	2.11°E, 47.96°N	-	2	-	[74]
Park Falls	pa	90.27°W, 45.94°N	14	9	8	[75]
Paris	pr	2.36°E, 48.85°N	1	4	-	[76]
Reunion Island	ra	55.48°E, 20.9°S	-	4	1	[77]
Rikubetsu	rj	143.77°E, 43.46°N	2	6	-	[78]
Sodankylä	so	26.63°E, 67.37°N	12	4	3	[79]
Tsukuba	tk	140.12°E, 36.05°N	53	11	-	[80]
Wollongong	wg	150.88°E, 34.41°S	4	10	1	[81]
Zugspitze	zs	10.98°E, 47.42°N	5	7	2	[82]

Note: Abb: Abbreviation; NC: Number of Collocations.

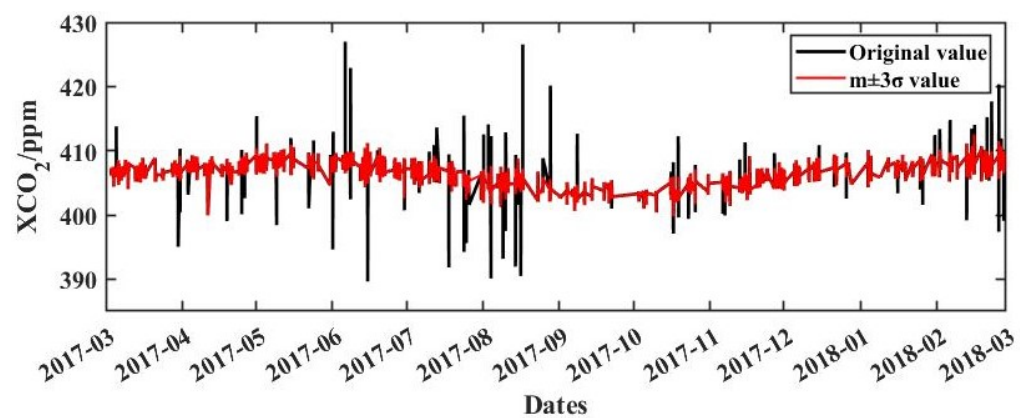


Figure 2. The original values of the Burgos site (bu) and the values after removing anomalies using the 3σ method are compared from March 2017 to March 2018.

2.2.2. Spatiotemporal Collocation Criterion for Intercomparison among Satellites

Table 1 illustrates the differences in footprint (spatial resolution) between the three carbon satellites. To facilitate their intercomparison, we calculated the counts of values and XCO₂ within each 1° × 1° spatial resolution grid. This choice aligns with the typical resolution used in most global models, which is 1° × 1°. Our approach involved the following steps: (1) We counted the number of data points within each 1° × 1° spatial range and sum points at the same latitude to analyze differences at varying latitudes for all three satellites. (2) For XCO₂, we first identified all XCO₂ values within each 1° × 1° range and then computed their average to obtain grid-level values. We also calculated the mean values of XCO₂ and standard deviations at different latitudes. (3) When analyzing the difference in XCO₂ (ΔXCO₂) between two satellites, we directly employed the difference method as shown in Equation (1) for each corresponding grid. To compare differences across different latitude bands, we averaged the differences of all grids within each latitude band and examined their variation with latitude. (4) Regarding the time scale, we analyzed the point counts and XCO₂ values of each satellite in four periods (seasons): December, January, February (DJF); March, April, May (MAM); June, July, August (JJA); and September, October, November (SON).

$$\Delta XCO_2 = XCO_{2s1} - XCO_{2s2} \quad (1)$$

where s1 and s2 represent any two satellites in GOT that we use to calculate their XCO₂ difference.

2.2.3. Matching Criteria for Satellites and TCCON

When matching the XGOT data with TCCON, we followed these steps: (1) Spatial Matching: Initially, we identified the location of each TCCON site. Next, we centered each point within a 1° × 1° spatial range and retrieved the XCO₂ values from the satellites within that range. These values were then averaged to create a spatial match. (2) Temporal Matching: Given that there were fewer or even no matching points on a per-minute scale, we matched the satellite data with a time range of ±30 min based on the acquisition time at the TCCON site. These values were averaged to form the final value for matching with TCCON. (3) Averaging: Since TCCON data are high-frequency values, we averaged the TCCON data and matched satellite values every half hour, starting at 0:00 UTC on 1 March 2017, to obtain the final results for analysis. (4) Additionally, to assess the proximity of satellite values to TCCON data at hemispherical scale, we calculated the differences in matching pairs for the Northern Hemisphere (NH) and Southern Hemisphere (SH).

2.2.4. Disparity Assessment

We used four indices, namely coefficient of determination (R²), root mean square error (RMSE), expectation (\bar{x}), and standard deviation (σ) to evaluate the ΔXCO₂ from satellites and TCCON. The mathematical expressions for these indices are as follows:

$$R^2 = 1 - \frac{\sum_{i=1}^n (Y_i - \hat{Y}_i)^2}{\sum_{i=1}^n (Y_i - \bar{Y}_i)^2} \quad (2)$$

$$RMSE = \sqrt{\frac{1}{n} \sum_{i=1}^n (X_i - Y_i)^2} \quad (3)$$

where n represents the total matching number, X is the XCO₂ from the satellite, Y is the XCO₂ from TCCON, \hat{Y}_i is the predicted value of Y, and \bar{Y}_i is the mathematical expectation of Y.

Concerning \bar{x} and σ , they satisfy the formula for the normal distribution:

$$f(x) = \frac{1}{\sqrt{2\pi}\sigma} e^{-\frac{(x-\bar{x})^2}{2\sigma^2}} \quad (4)$$

where x is the differences of XCO_2 between TCCON and satellite from collocation, \bar{x} represents the mean value of ΔXCO_2 , and σ represents the standard deviation, respectively.

3. Results

3.1. Spatial Coverage Characteristics of XCO_2 from Satellites

GOT consists of different observation programs, leading to variability in the amount of observational data and spatial coverage. GOSAT employs discrete sampling points for its observations, limiting its ability to continuously monitor space and providing only limited spatial coverage. In contrast, OCO-2 and TANSAT use narrow-amplitude (10–25 km) continuous pixel observations facilitated by high-resolution raster spectroscopy. However, there is a noticeable observational gap area between their orbital paths [83]. Figure 3 displays the spatial distribution of the original scattered XCO_2 data, revealing significant disparities between the GOT platforms. GOSAT has a northeast–southwest orientation, while OCO-2 and TANSAT direct their observations in the northwest–southeast direction. Additionally, it is evident that GOSAT has the largest orbital gaps, followed by TANSAT, whereas OCO-2's annual XCO_2 data can almost cover the entire terrestrial area. Since the inversion algorithm of TANSAT is primarily for land areas, there is no coverage over the oceans.

Figure 4a1–a12 displays the spatial distribution of point counts within each $1^\circ \times 1^\circ$ grid for the three satellites in four periods. Figure 4b1–b12 shows the total counts of XCO_2 points in each latitude band. It is important to note that, due to the extensive volume of data from OCO-2, we applied a logarithmic transformation with a base of 100 to map the spatial distribution of scatter counts.

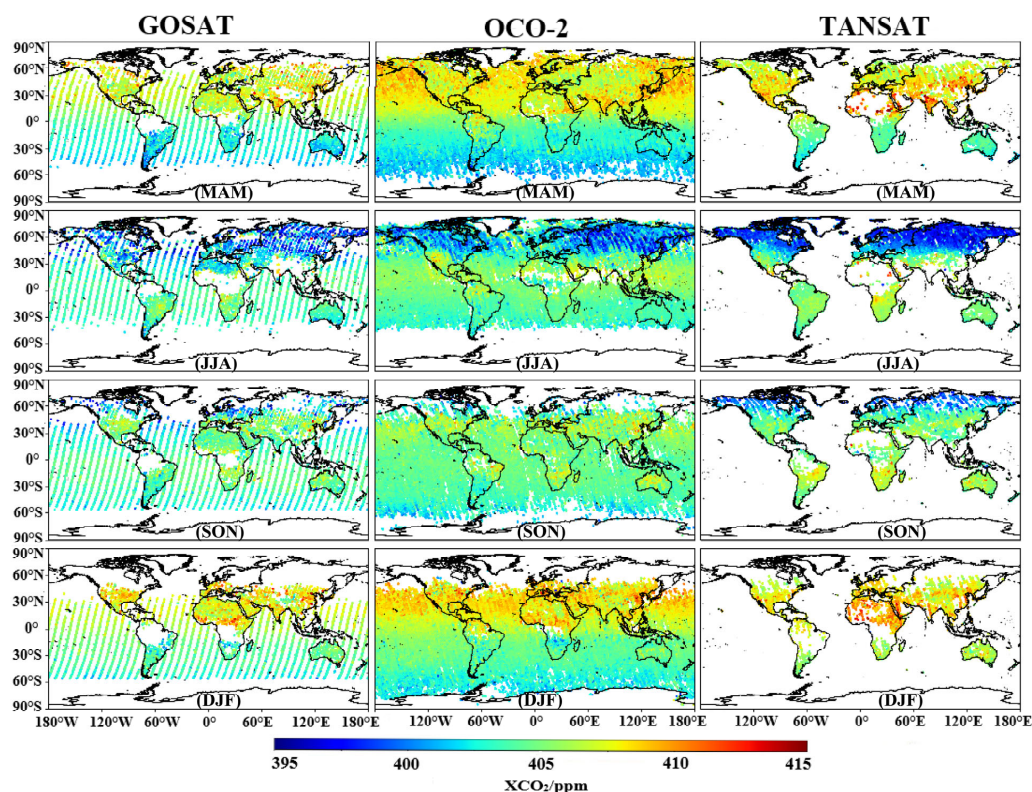


Figure 3. Scatter plot of the original XCO_2 data from the three satellites from March 2017 to February 2018. MAM: March, April, May; JJA: June, July, August; SON: September, October, November; DJF: December, January, February.

From the perspective of the spatial distribution of point counts, we can observe a significant degree of similarity among the GOT satellites, except in northern South America,

where GOSAT has a lower volume of XCO₂ data in all four periods. Similarly, TANSAT exhibits a lower volume of XCO₂ data in northern Africa during MAM, JJA, and SON.

When examining the counts in each latitude band, the GOT satellites show consistent distribution patterns with seasonal variations. For example, except for the Antarctic and Arctic regions, it is evident that all the satellites have limited data near the equator throughout the four periods, while data volume peaks in the NH and SH. In the NH, these peaks are predominantly concentrated within the latitudinal range of 30–45°N. Meanwhile, in the SH, the peaks are primarily concentrated between 20–30°S.

There are also disparities in the distribution of XCO₂ counts between the GOT satellites. Firstly, the XCO₂ data volume from OCO-2 is approximately 100 times larger than that of the other two satellites, and TANSAT's data volume is roughly twice that of GOSAT. Secondly, GOSAT and OCO-2 exhibit similar data distribution patterns across all four periods, whereas the TANSAT satellite shows significant variations in data quantity distribution. Notably, TANSAT's data volume reaches its peak during JJA and experiences a significant reduction during DJF. Thirdly, during JJA, TANSAT's data shows the highest volume around 70°N, a characteristic not exhibited by GOSAT and OCO-2. Finally, during DJF, TANSAT's data is scarce in the SH.

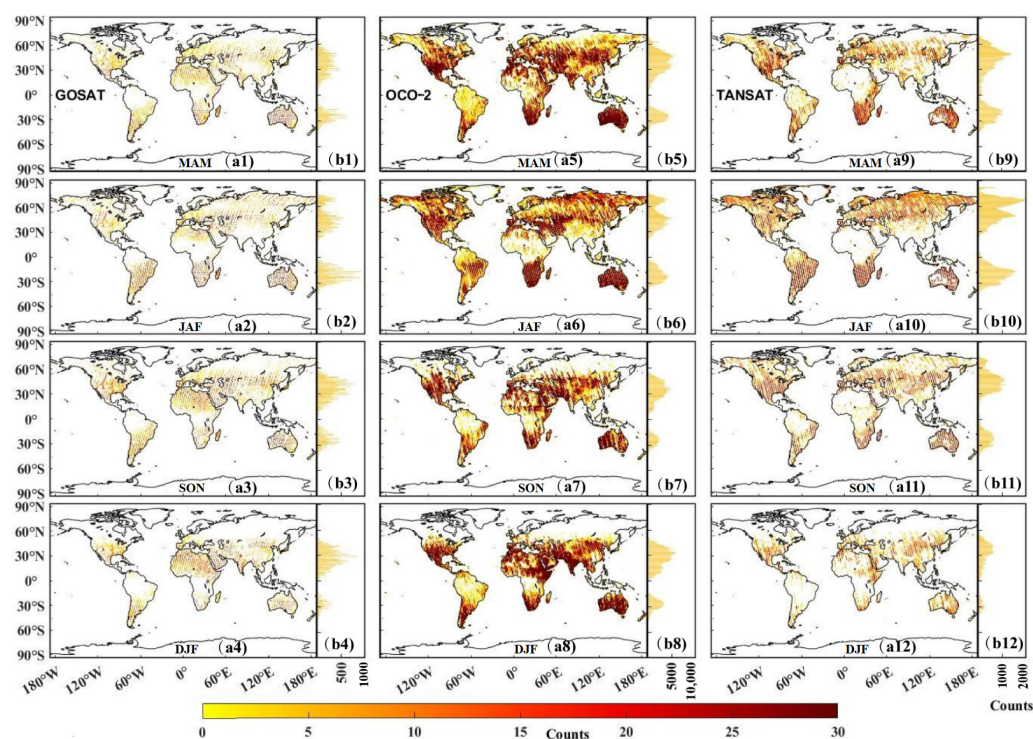


Figure 4. Spatial distribution of the number of XCO₂ points in 1° × 1° grids for GOSAT, OCO-2, and TANSAT in four periods (a1–a12) and the sum values of all grids in the same latitude band at 1° intervals (b1–b12).

3.2. The Intercomparison of XCO₂ from Satellites

3.2.1. Comparison of XCO₂: Seasonal, Spatial, and Latitudinal Aspects

Figure 5 compares the XGOT from seasonal, spatial, and latitudinal aspects. We initially evaluated the XGOT data in four periods. Figure 5a illustrates that XGOT exhibits a consistent seasonal variation pattern across all four periods. Specifically, XGOT has the lowest values in JJA (402.72 ppm, 403.76 ppm, and 403.74 ppm for GOT, respectively), followed by SON (403.39 ppm, 4.4.05 ppm, and 404.07 ppm), with the highest values occurring in DJF (405.74 ppm, 405.98 ppm, and 407.14 ppm). Furthermore, the XCO₂ values of TANSAT are consistently higher than those of OCO-2 throughout all periods, while GOSAT consistently exhibits the lowest values. Moreover, the standard error of TANSAT is

the largest, while OCO-2 has the smallest standard error, reflecting the relative consistency of the XCO₂ data to some extent.

From a spatial distribution perspective (Figure 5b1–b12), it is evident that XGOT exhibits similar spatial distribution characteristics. In MAM and DJF, human activities such as industrial activities and fossil fuel combustion contribute to a noticeable increase in global CO₂ concentration in the NH compared to the SH. However, with the onset of JJA, the photosynthetic efficiency of terrestrial vegetation in the NH leads to a substantial reduction in XCO₂ values, effectively reflecting the ‘carbon sequestration’ effect of ecosystems with seasonal changes.

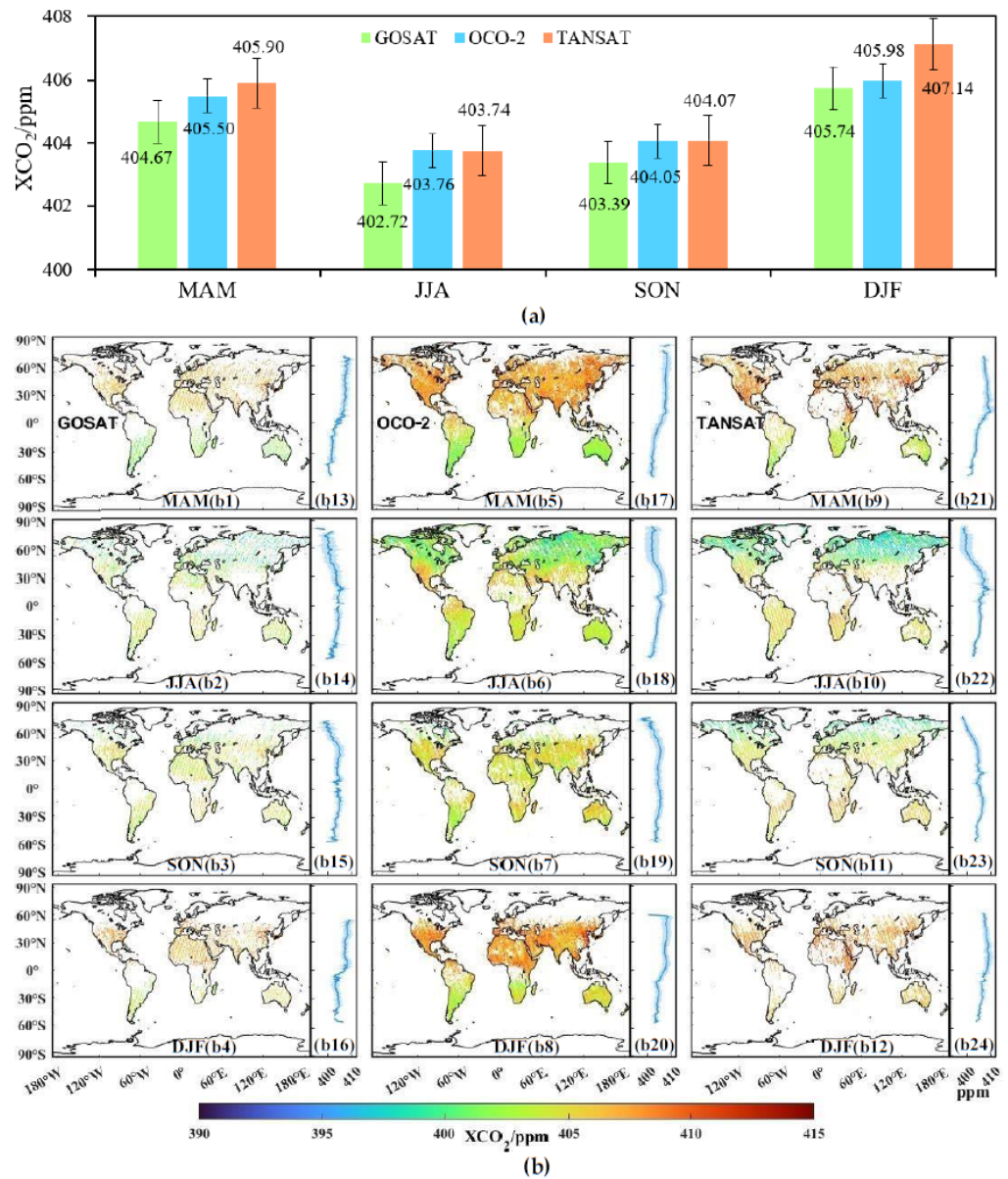


Figure 5. (a) The mean value of XCO₂ for four periods of GOSAT, OCO-2, and TANSAT; the black lines above the histogram represent the standard error of XCO₂ for each satellite during each period. (b) The spatial distribution of XCO₂. (b1–b12) The spatial distribution of XCO₂ on a 1° × 1° grid for four periods of three satellites. In (b13–b24), the dark blue line represents the average value of XCO₂ in latitudes with 1° intervals, and the light blue area indicates one standard deviation on either side of the mean value.

Analyzing XGOT in terms of latitude at 1° intervals (Figure 5b13–b24), we observed some common characteristics in all periods. For instance, during MAM and DJF, XCO_2 values in the NH are higher than those in the SH. Additionally, in MAM and JJA, XCO_2 values in the NH are slightly lower than those in the SH. Moreover, all three satellites indicate that the standard deviation of XCO_2 in the NH is greater than that in the SH during all periods (the area shaded in light blue is larger in the NH), indicating a larger dispersion of XCO_2 data in the NH. Simultaneously, small differences within the XGOT data have emerged. For example, in the NH during MAM and DJF, XGOT gradually increases northward overall, with TANSAT having a reduction between $30\text{--}60^\circ\text{N}$ when compared to the other two satellites. Moreover, GOSAT's XCO_2 data exhibit more variability across all latitudes, which may be a feature of the discrete sampling that GOSAT uses.

3.2.2. Comparison of ΔXCO_2 : Seasonal, Spatial, and Latitudinal Aspects

Figure 6 compares the ΔXCO_2 from seasonal, spatial, and latitudinal aspects between satellites. Figure 6a reveals that ΔXCO_2 of GOT ($\Delta XGOT$) remains relatively small (<1.5 ppm) throughout all periods. However, it exhibits some seasonal variation, with the difference being more pronounced in MAM and DJF (the biggest difference was between GOSAT and TANSAT at -1.33 ppm and -1.43 ppm, respectively) compared to JJA (the biggest difference between GOSAT and OCO-2: -0.95 ppm) and SON (the biggest difference between GOSAT and TANSAT: 0.84 ppm). Additionally, ΔXCO_2 between GOSAT and TANSAT shows significance across all periods (highlighted in purple), with an average annual difference of -1.13 ppm. The difference between OCO-2 and TANSAT is the smallest, except in DJF, with an average annual ΔXCO_2 of -0.47 ppm. The average annual ΔXCO_2 between GOSAT and OCO-2 is -0.62 ppm.

The spatial distribution maps of $\Delta XGOT$ were calculated to analyze their spatial differences (Figure 6b1–b12). Overall, the ΔXCO_2 between GOSAT and the other satellites exhibits similar characteristics in all four periods, with relatively small differences and no significant seasonal changes. However, there is some seasonal variation and variability in ΔXCO_2 between OCO-2 and TANSAT. During JJA in the NH, TANSAT's XCO_2 values were higher than OCO-2, and a similar phenomenon occurred in SON, albeit with weaker intensity.

To compare $\Delta XGOT$ at different latitudes, we calculated the mean ΔXCO_2 for each latitude band at 1° intervals (Figure 6b13–b24). In general, the ΔXCO_2 across latitude bands for all three satellites remained within ± 4 ppm. The difference between GOSAT and OCO-2 was the smallest, especially during DJF, suggesting that these two satellites exhibited greater consistency in their XCO_2 values. In contrast, ΔXCO_2 between TANSAT and both GOSAT and OCO-2 was much larger. The ΔXCO_2 between GOSAT and OCO-2 was predominantly negative (Figure 6b13–b16) in all four periods, indicating that GOSAT's XCO_2 values were consistently lower than those of OCO-2. GOSAT's XCO_2 values were also consistently lower than those of TANSAT throughout the year, and this difference was more pronounced compared to OCO-2. However, the difference between OCO-2 and TANSAT exhibited noticeable seasonal and latitudinal variations. For example, in MAM and DJF, ΔXCO_2 was primarily negative, indicating that TANSAT's values were larger than OCO-2 in these two periods. However, in JJA and SON there were differences between the NH and SH. In the NH (e.g., $45^\circ\text{--}75^\circ\text{N}$), ΔXCO_2 was positive, indicating that OCO-2's values were larger than TANSAT's. In the SH (e.g., $0^\circ\text{--}60^\circ\text{S}$), ΔXCO_2 was negative, indicating that OCO-2's values were smaller than TANSAT's.

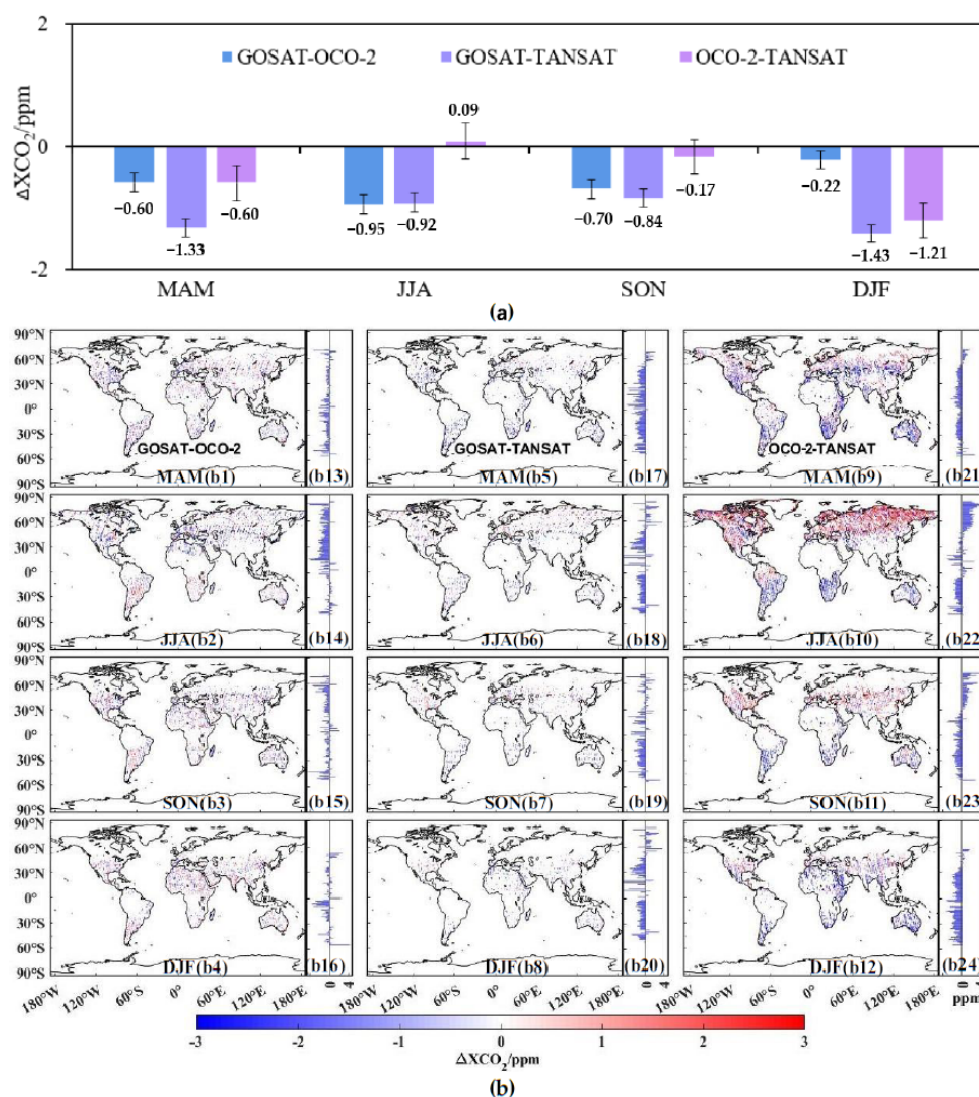


Figure 6. (a) The mean value of ΔXCO_2 for four periods of GOSAT, OCO-2, and TANSAT with standard error. The red line is the mean value of ΔXCO_2 of three satellites per period. (b1–b12) is the spatial distribution of ΔXCO_2 on a $1^\circ \times 1^\circ$ grid for four periods of three satellites. In (b13–b24), the blue bar graph represents the average value of ΔXCO_2 in latitude bands with 1° intervals.

3.3. Evaluation of ΔXCO_2 between Satellites and TCCON

3.3.1. Evaluation of ΔXCO_2 at Annual Scale

TCCON serves as a valuable source of ground-based data for validating satellite XCO_2 . Figure 7a1–a3 displays the validation plot of TCCON XCO_2 (XTCCON) against the matched XGOT data. GOSAT had the largest number of collocations ($N = 650$), while TANSAT had the least amount of data ($N = 52$). The fitted lines for the collocation data of all three satellites closely follow a 1:1 relationship, indicating that the XCO_2 obtained from satellite inversions is highly accurate. When analyzing the two parameters, R^2 and RMSE, TANSAT exhibited the highest accuracy (with the largest R^2 of 0.880 and the smallest RMSE of 1.055), followed by OCO-2 ($R^2 = 0.817$, RMSE = 1.067), and GOSAT demonstrated the lowest accuracy with an R^2 of 0.808 and an RMSE of 1.226.

Figure 7b1–b3 displays the frequency distribution of ΔXCO_2 , the difference between TCCON XCO_2 and satellite-derived XCO_2 . The frequency distributions of ΔXCO_2 are all normally transformed and fitted to the line using Equation (4). All ΔXCO_2 values are within the range of ± 4 ppm. GOSAT had an \bar{x} value of 0.319, which is greater than 0, suggesting that GOSAT's inversion underestimates XCO_2 compared to TCCON. The \bar{x} values for OCO-2 and TANSAT are both less than 0, indicating that the inverted XCO_2

values from both satellites are higher than those of TCCON. In terms of \bar{x} and σ parameters, OCO-2 exhibited the highest XCO₂ accuracy (\bar{x} is closest to 0 and σ is smallest), followed by TANSAT, while GOSAT had the lowest accuracy.

3.3.2. Evaluation of Δ XCO₂ at Seasonal and Hemispheric Scales

Considering the limited number of collocations, we used NH and SH averages to analyze the Δ XCO₂ between TCCON and the satellites during all periods. As depicted in Figure 8, the Δ XCO₂ values between TCCON and the satellites exhibited hemispheric divergence and seasonal variability. It is worth noting that TANSAT had no matched pair data in the SH during DJF. Overall, the satellites had more matches with TCCON in the NH, resulting in a more scattered Δ XCO₂ pattern (Figure 8a1–c4). Regarding the disparities between the NH and SH (Figure 8d1–d4), TANSAT showed the largest disparity, as indicated by the green bars changing direction between the hemispheres (Figure 8d1,d2) and displaying a substantial difference (Figure 8d3). In contrast, OCO-2 exhibited the smallest Δ XCO₂ between the NH and SH, with orange bars clustered near Δ XCO₂ = 0 (Figure 8d1–d4). Concerning seasonal variability (Figure 8d1–d4), the satellites were closest to TCCON values in JJA and SON but showed more significant differences from TCCON values in MAM and SON.

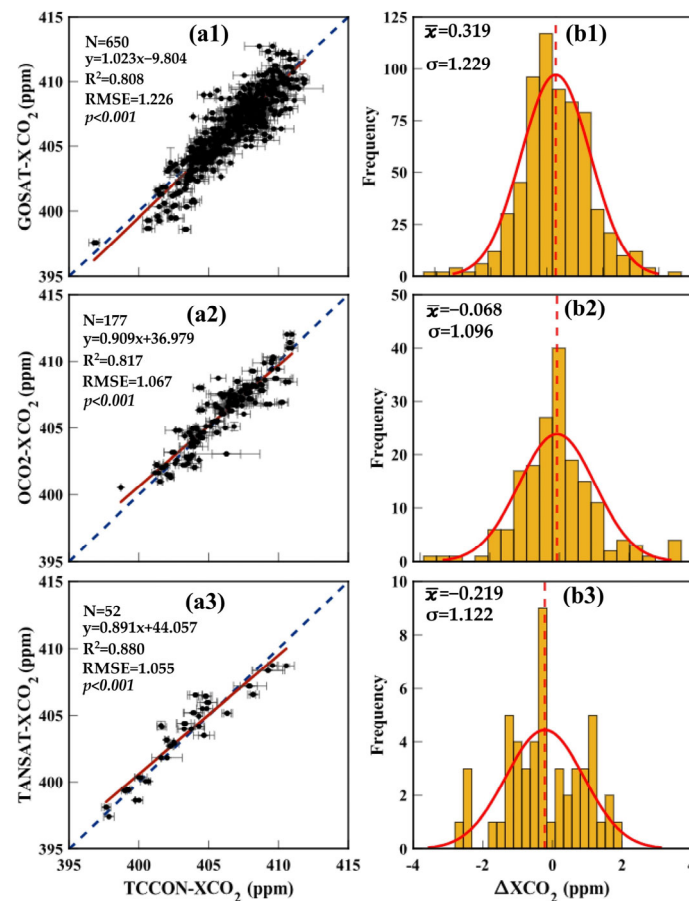


Figure 7. Scatter plot of the collocations of TCCON and XCO₂ from GOSAT (a1), OCO-2 (a2), and TANSAT (a3), using the $1^\circ \times 1^\circ$ and ± 30 min coincidence criteria. The blue dashed line is the one-to-one reference line, and the dark red solid line is the fitted line for the scatter with the corresponding regression formula shown in the Figure. N represents the number of matched collocations, R^2 represents the determination coefficient, and RMSE is the root mean square error. (b1–b3) Plots of the frequency distribution of Δ XCO₂ for TCCON versus the three satellites. The red solid line is the fitted line of the frequency distribution using Equation (4), the red dashed line corresponds to the \bar{x} value (expectation) in the plot, and σ is the standard deviation.

Regarding XGOT, TANSAT displayed significantly larger ΔXCO_2 values compared to the other satellites in MAM and DJF, indicating that TANSAT had lower values than TCCON in these two periods. However, in SON, ΔXCO_2 was smaller compared to the two other satellites, indicating that the XCO_2 values were higher than those of TCCON in this period. For GOSAT, all four periods exhibited $\Delta XCO_2 > 0$ (c), suggesting that its values were lower than those of TCCON. For OCO-2, $\Delta XCO_2 < 0$ in most periods, except for $\Delta XCO_2 > 0$ in JJA, indicating that it was underestimated in JJA and overestimated during other periods compared to TCCON, but the degree of underestimation and overestimation was relatively low.

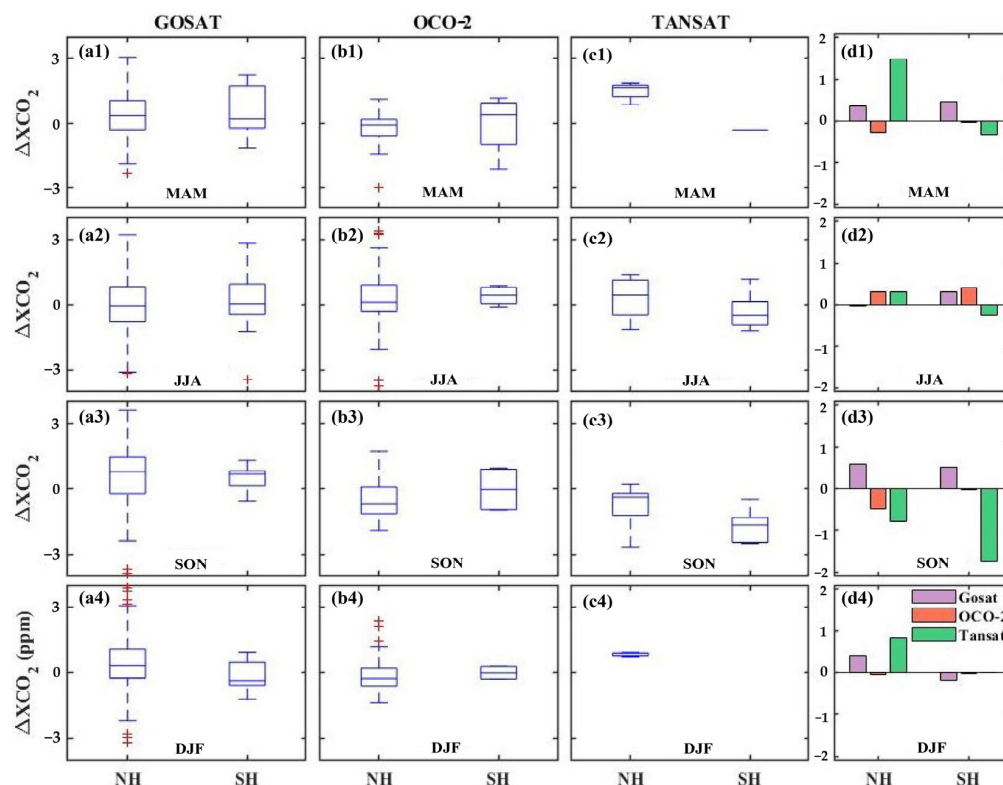


Figure 8. Data distribution of XCO_2 differences (ΔXCO_2) between TCCON and GOSAT, OCO-2, and TANSAT over four periods and the NH and SH (a1–c4). NH: Northern Hemisphere, SH: Southern Hemisphere. Note: The box has three lines, from bottom to top, referring to the quarter-quartile, median, and three-quarter-quartile. The top line is the maximum value in the non-anomalous range, the bottom line is the minimum value in the non-anomalous range, and the red cross symbols are the abnormal values. (d1–d4) The mean values of ΔXCO_2 over four periods in the NH and SH. TANSAT has no matching data for the SH in DJF.

4. Discussion and Conclusions

4.1. Discussion and Recommendation

Analysis of XCO_2 data frequently involves the comparison of observational data collected from multiple satellite platforms. Investigating the disparities between them to understand the global spatial distribution of CO_2 has important implications for insights into mitigation measures. Previously, extensive studies have been conducted in this area. In this context, our study adds a comparative analysis to the existing findings. Our results revealed that GOSAT had the lowest XCO_2 values, while TANSAT had the highest XCO_2 values as illustrated in Figure 5a. Moreover, the annual difference between GOSAT and OCO-2 was -0.62 ppm as demonstrated in Figure 6a. A similar result was reported previously [84]; the authors found the mean biases and standard deviations of GOSAT and OCO-2 are -0.57 ± 3.33 ppm over land. In addition, it was found that the GOSAT and

OCO-2 XCO₂ retrievals agree well in general, with a mean bias \pm standard deviation of -0.21 ± 1.3 ppm [36]. These results were in line with the previous studies.

In the context of TCCON evaluation, we chose spatial and temporal collocation criteria: a $1^\circ \times 1^\circ$ box with TCCON at its center and within 30 min. The upside of such a choice is the avoidance of additional collocation errors in our comparison results, and this criterion is consistent with the spatiotemporal resolution of the assimilated data required for our subsequent studies. The downside is a very limited dataset which effectively limits the analysis to seasonal, NH/SH aggregated data only. Another potential source of bias is that with strict criteria only a handful of stations effectively dominate the dataset, erroneously assuming that these (sometimes very local) measurements represent an entire hemisphere. For example, if we look at GOSAT collocations 300 of the 650 (all) or 561 (NH) collocated data points originate from the city of Los Angeles (Caltech and Pasadena), a highly polluted urban site, confined within the Los Angeles basin, and thus hardly representative of an entire hemisphere.

Despite the drawbacks, this study found that the RMSE values for GOSAT, OCO-2, and TANSAT with respect to TCCON were 1.226 ppm, 1.067 ppm, and 1.055 ppm, respectively (as shown in Figure 7a1–a3). These results align with previous findings. For instance, a comparison of XCO₂ data from OCO-2 with TCCON reported RMSE differences of less than 1.5 ppm [85]. Similarly, XCO₂ measurements from GOSAT and OCO-2 were 1.8 ppm and 1.76 ppm higher than the FTS measurements within a $\pm 1^\circ$ range centered on the ground-based FTS site in Beijing [86]. In our study, while the XCO₂ values from OCO-2 were higher than XTCCON, GOSAT's XCO₂ was lower than XTCCON. It is worth noting that negative systematic biases were identified in the XCO₂ measurements from OCO-2 in nadir modes at most TCCON sites [9]. Our study revealed a systematic bias between OCO-2 and TCCON of 0.068 (as shown in Figure 7b2). These varying conclusions suggest that differences in results can be attributed to the use of different TCCON observations (e.g., the number of TCCON sites, and the algorithm version of TCCON data) for comparison. Additionally, variations in results can be linked to the temporal range of the data. Therefore, it is crucial to conduct comparisons with TCCON using continuous measurements to evaluate the quality of satellite-derived XCO₂ data throughout their missions.

When comparing XCO₂ differences with TCCON at a hemispherical scale in four periods, the limitations of collocations between TANSAT and TCCON result in higher variations in the two hemispheres compared to GOSAT and OCO-2. A comparison of XCO₂ data from OCO-2 with XTCCON using different latitude zones found that in the mid–low latitudes OCO-2 data yielded good results in filtering and bias correction. However, in the high latitudes of the NH and SH, bias correction still required improvement [39]. In the future, multi-year XCO₂ data from satellites should be used to evaluate differences with TCCON in different latitude bands, not just on a hemispheric scale.

Regarding comparisons across different latitude bands, we conducted an intercomparison of XGOT using latitude bands with a 1° interval. While our global-scale analysis showed that Δ XCO₂ between OCO-2 and TANSAT is small during JJA and SON (as depicted in Figure 6a), a more detailed examination revealed significant differences in Δ XCO₂ between the SH and NH (Figure 6b). In essence, the global perspective can mask regional variations in Δ XCO₂ due to the opposite signs of Δ XCO₂ between the hemispheres. This underscores the importance of conducting more detailed analyses to gain a more accurate understanding of the sources of data errors and establish a foundation of higher accuracy and reliability for future research and data applications.

Based on our current research findings, we propose several future research prospects. Firstly, we recommend an extended analysis of data over a longer period to obtain a comprehensive understanding of XCO₂ variability. Secondly, we advocate for an in-depth exploration of the sources of XCO₂ errors, focusing on factors such as latitude, surface properties, and the influence of aerosol scattering. This analysis has the potential to improve inversion algorithms and enhance product quality. Furthermore, we encourage the utilization of these data in assimilation systems for flux inversion. This could lead to

more accurate estimates of carbon flux and contribute valuable insights to the scientific community in resolving ongoing debates in flux estimation [32,83]. Our study plays a crucial role in evaluating how the integration of XGOT into assimilation systems influences the distribution of inversion flux results.

4.2. Conclusions

GOT have emerged as popular satellites for specialized global CO₂ distribution detection. This study conducts comprehensive cross-comparisons of ACOS_L2_Lite_FP V9r for GOSAT, OCO-2_L2_Lite_FP V10r for OCO-2, and IAPCAS V2.0 for TANSAT over land areas. The primary focus is on data quantity patterns and XCO₂ variability with spatial, seasonal, and 1° latitude interval variations. Moreover, to gauge the accuracy, TCCON data were employed to assess GOT's performance at annual, seasonal, and hemispheric scales. The principal findings can be summarized as follows:

Observational Strategies and Spatial Coverage Differences: Noticeable differences exist in the observational strategies and spatial coverage of the three satellites. GOSAT relies on discrete sampling points, limiting its coverage and leading to significant orbital gaps. Conversely, OCO-2 and TANSAT employ continuous pixel-level observations, resulting in more extensive coverage. Particularly noteworthy is OCO-2's data volume, which is a hundredfold greater than the combined output of the other two satellites, while TANSAT records a data volume twice that of GOSAT. All three satellites exhibit data volume peaks between 30–45°N and 20–30°S, with relatively fewer data points near the equator. With the exception of TANSAT, which shows limited data during DJF, data volumes remain relatively consistent across all periods.

Seasonal XCO₂ Measurements: The XGOT display similar seasonal variations, with the lowest values during JJA (402.72–403.74 ppm) and the highest values during DJF (405.74–407.14 ppm). TANSAT consistently records the highest XCO₂ values within each period, while GOSAT consistently reports the lowest values. When assessing latitude bands, the highest XCO₂ values for all satellites are observed within the 0–30°N range. During MAM and DJF, the NH exhibits higher concentrations than the SH, whereas the reverse pattern is observed during JJA and SON.

Inter-satellite ΔXCO₂ Comparisons: The study reveals that the lowest ΔXCO₂ values between GOT are observed in SON (the biggest difference was −0.84 ppm between GOSAT and TANSAT), while the highest occurs in DJF (the biggest difference was −1.33 ppm between GOSAT and TANSAT). The ΔXCO₂ value between OCO-2 and TANSAT is the smallest (−0.47 ppm), whereas the ΔXCO₂ of GOSAT and TANSAT appears the highest (−1.13 ppm). The ΔXCO₂ between GOSAT and the other two satellites uniformly underestimates values across different latitude bands. However, the ΔXCO₂ between OCO-2 and TANSAT exhibits latitude band variations, particularly during JJA and SON. Specifically, in the NH during JJA and SON, TANSAT values are noticeably higher than OCO-2, while the SH reflects the opposite phenomenon. Importantly, when comparing data from different satellite sources, comprehensive analyses at appropriate temporal and spatial scales are crucial for accurate results. Furthermore, all three satellites demonstrate good accuracy when compared with TCCON data, with R² values exceeding 0.8, and the maximum RMSE observed in GOSAT is 1.226 ppm.

These findings collectively enhance our understanding of the role of GOT data in the global carbon cycle, enriching insights into carbon cycle dynamics and aiding climate change mitigation efforts. Despite some differences among GOT, they all provide accurate inversion results. This study offers a detailed analysis of the consistency of XCO₂ products from GOT, contributing to the analysis of global CO₂ concentration characteristics. Additionally, it provides valuable references for selecting data for incorporation into assimilation inversion systems and supports attribution analyses of spatial flux inversion.

Author Contributions: Conceptualization, B.C.; methodology, J.F.; software, J.F.; validation, B.C., H.Z. and M.G.; formal analysis, J.F., H.Z. and T.M.G.; investigation, J.F. and C.L.; resources, B.C.; data curation, J.F., X.Z. and S.L.; writing—original draft preparation, J.F.; writing—review and

editing, B.C., J.F., X.Z., H.Z. and A.D.; visualization, J.F. and S.L.; supervision, B.C. and H.Z.; project administration, B.C.; funding acquisition, H.Z. All authors have read and agreed to the published version of the manuscript.

Funding: This research was funded by the National Natural Science Foundation of China (No. 41890854, No. 41771114), the Chinese Academy of Sciences Class A Strategic Pilot Science and Technology Project (No. XDA23100202), and the Innovation Project of LREIS (No. KPI005).

Data Availability Statement: Regarding data availability, a detailed explanation is provided in Section 2.1, along with the website for data download. For more information, please refer to Section 2.1.

Acknowledgments: We acknowledge the ACOS GOSAT, ACOS OCO-2, and TANSAT projects for providing the XCO₂ data archives. The GOSAT and OCO-2 data were obtained from the OCO-2 data archive maintained at the NASA Goddard Earth Science Data and Information Services Center. The TANSAT data were obtained from Xingying Zhang at National Satellite Meteorological Center, China Meteorological Administration. The TCCON data were obtained from the TCCON Data Archive hosted by CaltechDATA at <https://tccondata.org> (accessed on 8 July 2023). We also express our gratitude to the TCCON Project, especially for TCCON PIs for the TCCON measurements at the stations of Anmyeondo, Bialystok, Burgos, Caltech, Darwin, Dryden, East Trout Lake, Eureka, Garmisch, Hefei, Izana, Pasadena, Saga, Karlsruhe, Lauder, Ny-Ålesund, Lamont, Orléans, Park Falls, Paris, Reunion Island, Rikubetsu, Sodankylä, Tsukuba, Wollongong, and Zugspitze. The Paris TCCON site has received funding from Sorbonne Université, the French research center CNRS, the French space agency CNES, and Région Île-de-France. The TCCON stations at Rikubetsu and Burgos are supported in part by the GOSAT series project. Local support for Burgos is provided by the Energy Development Corporation (EDC, Philippines). Darwin and Wollongong TCCON stations are supported by ARC grants DP160100598, LE0668470, DP140101552, DP110103118, and DP0879468.

Conflicts of Interest: The authors declare no conflict of interest.

References

1. Lenzen, M. Global Warming Effect of Leakage from CO₂ Storage. *Crit. Rev. Environ. Sci. Technol.* **2011**, *41*, 2169–2185. [[CrossRef](#)]
2. Al-Ghussain, L. Global warming: Review on driving forces and mitigation. *Environ. Prog. Sustain. Energy* **2019**, *38*, 13–21. [[CrossRef](#)]
3. Sun, L.Y.; Wang, M.H. Global warming and global dioxide emission: An empirical study. *J. Environ. Manag.* **1996**, *46*, 327–343. [[CrossRef](#)]
4. Williams, R.G.; Roussinov, V.; Goodwin, P.; Resplandy, L.; Bopp, L. Sensitivity of Global Warming to Carbon Emissions: Effects of Heat and Carbon Uptake in a Suite of Earth System Models. *J. Clim.* **2017**, *30*, 9343–9363. [[CrossRef](#)]
5. IPCC. *Climate Change 2013: The Physical Science Basis. Contribution of Working Group I to the Fifth Assessment Report of the Intergovernmental Panel on Climate Change*; IPCC: Cambridge, UK; New York, NY, USA, 2013.
6. Cao, J.; Ho, M.; Liu, Q.F. Analyzing multi-greenhouse gas mitigation of China using a general equilibrium model. *Environ. Res. Lett.* **2023**, *18*, 025001. [[CrossRef](#)]
7. Wen, Z.G.; Di, J.H.; Yu, X.W.; Zhang, X. Analyses of CO₂ mitigation roadmap in China's power industry: Using a Backcasting Model. *Appl. Energy* **2017**, *205*, 644–653. [[CrossRef](#)]
8. Crisp, D. Retrieving CO₂ from GOSAT observations using the ACOS/OCO-2 retrieval algorithm. In Proceedings of the 39th COSPAR Scientific Assembly, Mysore, India, 14–22 July 2012; p. 377.
9. Bi, Y.; Wang, Q.; Yang, Z.; Chen, J.; Bai, W. Validation of Column-Averaged Dry-Air Mole Fraction of CO₂ Retrieved from OCO-2 Using Ground-Based FTS Measurements. *J. Meteorol. Res.* **2018**, *32*, 433–443. [[CrossRef](#)]
10. O'Dell, C.W.; Connor, B.; Bosch, H.; O'Brien, D.; Frankenberg, C.; Castano, R.; Christi, M.; Crisp, D.; Eldering, A.; Fisher, B.; et al. The ACOS CO₂ retrieval algorithm—Part 1: Description and validation against synthetic observations. *Atmos. Meas. Tech.* **2012**, *5*, 99–121. [[CrossRef](#)]
11. Liu, Y.; Yang, D.; Cai, Z. A retrieval algorithm for TanSat XCO₂ observation: Retrieval experiments using GOSAT data. *Chin. Sci. Bull.* **2013**, *58*, 1520–1523. [[CrossRef](#)]
12. Liu, Y.; Cai, Z.N.; Yang, D.X.; Zheng, Y.Q.; Duan, M.Z.; Lu, D.R. Effects of spectral sampling rate and range of CO₂ absorption bands on XCO₂ retrieval from TanSat hyperspectral spectrometer. *Chin. Sci. Bull.* **2014**, *59*, 1485–1491. [[CrossRef](#)]
13. Zhou, M.; Zhang, X.; Wang, P.; Wang, S.; Guo, L.; Hu, L. XCO₂ satellite retrieval experiments in short-wave infrared spectrum and ground-based validation. *Sci. China-Earth Sci.* **2015**, *58*, 1191–1197. [[CrossRef](#)]
14. Yoshida, Y.; Kikuchi, N.; Morino, I.; Uchino, O.; Oshchepkov, S.; Bril, A.; Saeki, T.; Schutgens, N.; Toon, G.C.; Wunch, D.; et al. Improvement of the retrieval algorithm for GOSAT SWIR XCO₂ and XCH₄ and their validation using TCCON data. *Atmos. Meas. Tech.* **2013**, *6*, 1533–1547. [[CrossRef](#)]

15. Yang, D.; Boesch, H.; Liu, Y.; Somkuti, P.; Cai, Z.; Chen, X.; Di Noia, A.; Lin, C.; Lu, N.; Lyu, D.; et al. Toward High Precision XCO₂ Retrievals from TanSat Observations: Retrieval Improvement and Validation Against TCCON Measurements. *J. Geophys. Res. Atmos.* **2020**, *125*, e2020JD032794. [[CrossRef](#)] [[PubMed](#)]
16. Someya, Y.; Yoshida, Y.; Ohyama, H.; Nomura, S.; Kamei, A.; Morino, I.; Mukai, H.; Matsunaga, T.; Laughner, J.L.; Velasco, V.A.; et al. Update on the GOSAT TANSO-FTS SWIR Level 2 retrieval algorithm. *Atmos. Meas. Tech.* **2023**, *16*, 1477–1501. [[CrossRef](#)]
17. David, L.; Breon, F.-M.; Chevallier, F. XCO₂ estimates from the OCO-2 measurements using a neural network approach. *Atmos. Meas. Tech.* **2021**, *14*, 117–132. [[CrossRef](#)]
18. Liu, R.-X.; Zhang, X.-Y.; Liu, J.; Liu, Y.-G. A Spatial-Temporal Distribution Characteristics Study on The Atmospheric Carbon Dioxide Observed By Gosat Satellite Remote Sensing. *J. Trop. Meteorol.* **2015**, *21*, 408–416.
19. Golkar, F.; Mousavi, S.M. Variation of XCO₂ anomaly patterns in the Middle East from OCO-2 satellite data. *Int. J. Digit. Earth* **2022**, *15*, 1219–1235. [[CrossRef](#)]
20. Mustafa, F.; Bu, L.; Wang, Q.; Ali, M.; Bilal, M.; Shahzaman, M.; Qiu, Z. Multi-Year Comparison of CO₂ Concentration from NOAA Carbon Tracker Reanalysis Model with Data from GOSAT and OCO-2 over Asia. *Remote Sens.* **2020**, *12*, 2498. [[CrossRef](#)]
21. Hammerling, D.M.; Michalak, A.M.; O'Dell, C.; Kawa, S.R. Global CO₂ distributions over land from the Greenhouse Gases Observing Satellite (GOSAT). *Geophys. Res. Lett.* **2012**, *39*, L08804. [[CrossRef](#)]
22. Jiang, F.; Ju, W.; He, W.; Wu, M.; Wang, H.; Wang, J.; Jia, M.; Feng, S.; Zhang, L.; Chen, J.M. A 10-year global monthly averaged terrestrial net ecosystem exchange dataset inferred from the ACOS GOSAT v9 XCO₂ retrievals (GCAS2021). *Earth Syst. Sci. Data* **2022**, *14*, 3013–3037. [[CrossRef](#)]
23. Patra, P.K.; Hajima, T.; Saito, R.; Chandra, N.; Yoshida, Y.; Ichii, K.; Kawamiya, M.; Kondo, M.; Ito, A.; Crisp, D. Evaluation of earth system model and atmospheric inversion using total column CO₂ observations from GOSAT and OCO-2. *Prog. Earth Planet. Sci.* **2021**, *8*, 25. [[CrossRef](#)]
24. Philip, S.; Johnson, M.S.; Baker, D.F.; Basu, S.; Tiwari, Y.K.; Indira, N.K.; Ramonet, M.; Poulter, B. OCO-2 Satellite-Imposed Constraints on Terrestrial Biospheric CO₂ Fluxes Over South Asia. *J. Geophys. Res. Atmos.* **2022**, *127*, e2021JD035035. [[CrossRef](#)]
25. He, W.; Jiang, F.; Ju, W.; Chevallier, F.; Baker, D.F.; Wang, J.; Wu, M.; Johnson, M.S.; Philip, S.; Wang, H.; et al. Improved Constraints on the Recent Terrestrial Carbon Sink Over China by Assimilating OCO-2 XCO₂ Retrievals. *J. Geophys. Res. Atmos.* **2023**, *128*, e2022JD037773. [[CrossRef](#)]
26. Yang, D.; Zhang, H.; Liu, Y.; Chen, B.; Cai, Z.; Lü, D. Monitoring carbon dioxide from space: Retrieval algorithm and flux inversion based on GOSAT data and using CarbonTracker-China. *Adv. Atmos. Sci.* **2017**, *34*, 965–976. [[CrossRef](#)]
27. Jiang, F.; He, W.; Ju, W.; Wang, H.; Wu, M.; Wang, J.; Feng, S.; Zhang, L.; Chen, J.M. The status of carbon neutrality of the world's top 5 CO₂ emitters as seen by carbon satellites. *Fundam. Res.* **2022**, *2*, 357–366. [[CrossRef](#)]
28. Jiang, F.; Chen, J.M.; Zhou, L.X.; Ju, W.M.; Zhang, H.F.; Machida, T.; Ciais, P.; Peters, W.; Wang, H.M.; Chen, B.Z.; et al. A comprehensive estimate of recent carbon sinks in China using both top-down and bottom-up approaches. *Sci. Rep.* **2016**, *6*, 22130. [[CrossRef](#)] [[PubMed](#)]
29. Chevallier, F.; Broquet, G.; Zheng, B.; Ciais, P.; Eldering, A. Large CO₂ Emitters as Seen from Satellite: Comparison to a Gridded Global Emission Inventory. *Geophys. Res. Lett.* **2022**, *49*, e2021GL097540. [[CrossRef](#)] [[PubMed](#)]
30. Zhang, H.F.; Chen, B.Z.; van der Laan-Luijkx, I.T.; Chen, J.; Xu, G.; Yan, J.W.; Zhou, L.X.; Fukuyama, Y.; Tans, P.P.; Peters, W. Net terrestrial CO₂ exchange over China during 2001–2010 estimated with an ensemble data assimilation system for atmospheric CO₂. *J. Geophys. Res. Atmos.* **2014**, *119*, 3500–3515. [[CrossRef](#)]
31. Piao, S.L.; Ciais, P.; Lomas, M.; Beer, C.; Liu, H.Y.; Fang, J.Y.; Friedlingstein, P.; Huang, Y.; Muraoka, H.; Son, Y.H.; et al. Contribution of climate change and rising CO₂ to terrestrial carbon balance in East Asia: A multi-model analysis. *Glob. Planet. Change* **2011**, *75*, 133–142. [[CrossRef](#)]
32. Chen, B.; Zhang, H.; Wang, T.; Zhang, X. An atmospheric perspective on the carbon budgets of terrestrial ecosystems in China: Progress and challenges. *Sci. Bull.* **2021**, *66*, 1713–1718. [[CrossRef](#)]
33. Guerlet, S.; Butz, A.; Schepers, D.; Basu, S.; Hasekamp, O.P.; Kuze, A.; Yokota, T.; Blavier, J.F.; Deutscher, N.M.; Griffith, D.W.T.; et al. Impact of aerosol and thin cirrus on retrieving and validating XCO₂ from GOSAT shortwave infrared measurements. *J. Geophys. Res. Atmos.* **2013**, *118*, 4887–4905. [[CrossRef](#)]
34. Wang, Y.; Tian, X.; Chevallier, F.; Johnson, M.S.; Philip, S.; Baker, D.F.; Schuh, A.E.; Deng, F.; Zhang, X.; Zhang, L.; et al. Constraining China's land carbon sink from emerging satellite CO₂ observations: Progress and challenges. *Glob. Change Biol.* **2022**, *28*, 6838–6846. [[CrossRef](#)] [[PubMed](#)]
35. Zhang, L.L.; Yue, T.X.; Wilson, J.P.; Zhao, N.; Zhao, Y.P.; Du, Z.P.; Liu, Y. A comparison of satellite observations with the XCO(2) surface obtained by fusing TCCON measurements and GEOS-Chem model outputs. *Sci. Total Environ.* **2017**, *601–602*, 1575–1590. [[CrossRef](#)] [[PubMed](#)]
36. Kong, Y.; Chen, B.; Measho, S. Spatio-Temporal Consistency Evaluation of XCO₂ Retrievals from GOSAT and OCO-2 Based on TCCON and Model Data for Joint Utilization in Carbon Cycle Research. *Atmosphere* **2019**, *10*, 354. [[CrossRef](#)]
37. Liang, A.; Gong, W.; Han, G.; Xiang, C. Comparison of Satellite-Observed XCO₂ from GOSAT, OCO-2, and Ground-Based TCCON. *Remote Sens.* **2017**, *9*, 1033. [[CrossRef](#)]
38. Hong, X.; Zhang, P.; Bi, Y.; Liu, C.; Sun, Y.; Wang, W.; Chen, Z.; Yin, H.; Zhang, C.; Tian, Y.; et al. Retrieval of Global Carbon Dioxide from TanSat Satellite and Comprehensive Validation with TCCON Measurements and Satellite Observations. *IEEE Trans. Geosci. Remote Sens.* **2022**, *60*, 1–16. [[CrossRef](#)]

39. Liang, A.; Han, G.; Gong, W.; Yang, J.; Xiang, C. Comparison of Global XCO₂ Concentrations From OCO-2 With TCCON Data in Terms of Latitude Zones. *IEEE J. Sel. Top. Appl. Earth Obs. Remote Sens.* **2017**, *10*, 2491–2498. [[CrossRef](#)]
40. Zhang, H.; Chen, B.; Xu, G.; Yan, J.; Che, M.; Chen, J.; Fang, S.; Lin, X.; Sun, S. Comparing simulated atmospheric carbon dioxide concentration with GOSAT retrievals. *Sci. Bull.* **2015**, *60*, 380–386. [[CrossRef](#)]
41. Crisp, D.; Pollock, H.R.; Rosenberg, R.; Chapsky, L.; Lee, R.A.M.; Oyafuso, F.A.; Frankenberg, C.; O'Dell, C.W.; Bruegge, C.J.; Doran, G.B.; et al. The on-orbit performance of the Orbiting Carbon Observatory-2 (OCO-2) instrument and its radiometrically calibrated products. *Atmos. Meas. Tech.* **2017**, *10*, 59–81. [[CrossRef](#)]
42. Ran, Y.; Li, X. TanSat: A new star in global carbon monitoring from China. *Sci. Bull.* **2019**, *64*, 284–285. [[CrossRef](#)]
43. Liu, Y.; Wang, J.; Che, K.; Cai, Z.; Yang, D.; Wu, L. Satellite remote sensing of greenhouse gases: Progress and trends. *J. Remote Sens.* **2021**, *25*, 53–64. [[CrossRef](#)]
44. Suto, H.; Kataoka, F.; Kikuchi, N.; Knuteson, R.O.; Butz, A.; Haun, M.; Buijs, H.; Shiomi, K.; Imai, H.; Kuze, A. Thermal and near-infrared sensor for carbon observation Fourier transform spectrometer-2 (TANSO-FTS-2) on the Greenhouse gases Observing SATellite-2 (GOSAT-2) during its first year in orbit. *Atmos. Meas. Tech.* **2021**, *14*, 2013–2039. [[CrossRef](#)]
45. O'Dell, C.; Osterman, G. Retrievals of Carbon Dioxide from GOSAT Using the Atmospheric CO₂ Observations from Space (ACOS) Algorithm Level 2 Standard Product and Lite Data Product Data User's Guide, v9. 2020. Available online: https://docserver.gesdisc.eosdis.nasa.gov/public/project/OCO/ACOS_v9_DataUsersGuide.pdf (accessed on 6 August 2023).
46. Available online: <https://disc.gsfc.nasa.gov/> (accessed on 6 August 2023).
47. Merrelli, A.; Bennartz, R.; O'Dell, C.W.; Taylor, T.E. Estimating bias in the OCO-2 retrieval algorithm caused by 3-D radiation scattering from unresolved boundary layer clouds. *Atmos. Meas. Tech.* **2015**, *8*, 1641–1656. [[CrossRef](#)]
48. Crisp, D.; Atlas, R.M.; Breon, F.M.; Brown, L.R.; Burrows, J.P.; Ciaia, P.; Connor, B.J.; Doney, S.C.; Fung, I.Y.; Jacob, D.J.; et al. The orbiting carbon observatory (OCO) mission. In *Trace Constituents in the Troposphere and Lower Stratosphere*; Burrows, J.P., Thompson, A.M., Eds.; The Committee by Pergamon Press: New York, NY, USA, 2004; Volume 34, pp. 700–709.
49. Kong, Y.W.; Zheng, B.; Zhang, Q.; He, K.B. Global and regional carbon budget for 2015–2020 inferred from OCO-2 based on an ensemble Kalman filter coupled with GEOS-Chem. *Atmos. Chem. Phys.* **2022**, *22*, 10769–10788. [[CrossRef](#)]
50. Crisp, D.; O'Dell, C.; Eldering, A. Level 2 Full Physics Retrieval Algorithm Theoretical Basis. 2021. Available online: https://docserver.gesdisc.eosdis.nasa.gov/public/project/OCO/OCO_L2_ATBD.pdf (accessed on 6 August 2023).
51. Eldering, A.; O'Dell, C.W.; Wennberg, P.O.; Crisp, D.; Gunson, M.R.; Viatte, C.; Avis, C.; Braverman, A.; Castano, R.; Chang, A.; et al. The Orbiting Carbon Observatory-2: First 18 months of science data products. *Atmos. Meas. Tech.* **2017**, *10*, 549–563. [[CrossRef](#)]
52. Liu, Y.; Wang, J.; Yao, L.; Chen, X.; Cai, Z.; Yang, D.; Yin, Z.; Gu, S.; Tian, L.; Lu, N.; et al. The TanSat mission: Preliminary global observations. *Sci. Bull.* **2018**, *63*, 1200–1207. [[CrossRef](#)] [[PubMed](#)]
53. Liu, Y.; Yao, L.; Wang, J.; Yang, D. Application status of Chinese carbon satellite data. *Satell. Appl.* **2022**, *2022*, 46–50.
54. Yang, D.; Liu, Y.; Boesch, H.; Yao, L.; Di Noia, A.; Cai, Z.; Lu, N.; Lyu, D.; Wang, M.; Wang, J.; et al. A New TanSat XCO₂ Global Product towards Climate Studies. *Adv. Atmos. Sci.* **2020**, *38*, 8–11. [[CrossRef](#)]
55. Wunch, D.; Toon, G.C.; Blavier, J.F.L.; Washenfelder, R.A.; Notholt, J.; Connor, B.J.; Griffith, D.W.T.; Sherlock, V.; Wennberg, P.O. The Total Carbon Column Observing Network. *Philos. Trans. R. Soc. A Math. Phys. Eng. Sci.* **2011**, *369*, 2087–2112. [[CrossRef](#)]
56. Wunch, D.; Wennberg, P.O.; Toon, G.C.; Connor, B.J.; Fisher, B.; Osterman, G.B.; Frankenberg, C.; Mandrake, L.; O'Dell, C.; Ahonen, P.; et al. A method for evaluating bias in global measurements of CO₂ total columns from space. *Atmos. Chem. Phys.* **2011**, *11*, 12317–12337. [[CrossRef](#)]
57. Goo, T.Y.; Oh, Y.S.; Velazco, V.A. TCCON Data from Anmyeondo, South Korea, Release GGG2020R0. In *TCCON Data Archive*; CaltechDATA, California Institute of Technology: Pasadena, CA, USA, 2020.
58. Petri, C.; Deutscher, N.; Notholt, J.; Messerschmidt, J.; Weinzierl, C.; Warneke, T.; Grupe, P.; Katrynski, K. TCCON data from Bialystok, Poland, Release GGG2020R0. In *TCCON Data Archive*; CaltechDATA, California Institute of Technology: Pasadena, CA, USA, 2020.
59. Morino, I.; Velazco, V.A.; Hori, A.; Uchino, O.; Griffith, D.W.T. TCCON Data from Burgos, Philippines, Release GGG2020R0. In *TCCON Data Archive*; CaltechDATA, California Institute of Technology: Pasadena, CA, USA, 2020. [[CrossRef](#)]
60. Wennberg, P.O.; Wunch, D.; Roehl, C.; Blavier, J.F.; Toon, G.C.; Allen, N. TCCON Data from California Institute of Technology, Pasadena, California, USA, Release GGG2020R0. In *TCCON Data Archive*; CaltechDATA, California Institute of Technology: Pasadena, CA, USA, 2020. [[CrossRef](#)]
61. Deutscher, N.M.; Griffith, D.W.T.; Paton-Walsh, C.; Velazco, V.A.; Wennberg, P.O.; Blavier, J.F.; Washenfelder, R.A.; Yavin, Y.; Keppel-Aleks, G.; Toon, G.C. TCCON Data from Darwin (AU), Release GGG2020.R0. In *TCCON Data Archive*; CaltechDATA, California Institute of Technology: Pasadena, CA, USA, 2020. [[CrossRef](#)]
62. Iraci, L.; Podolske, J.; Roehl, C.; Wennberg, P.O.; Blavier, J.F.; Allen, N.; Wunch, D.; Osterman, G. TCCON Data from Armstrong Flight Research Center, Edwards, CA, USA, Release GGG2020R0. In *TCCON Data Archive*; CaltechDATA, California Institute of Technology: Pasadena, CA, USA, 2020. [[CrossRef](#)]
63. Wunch, D.; Mendonca, J.; Colebatch, O.; Allen, N.; Blavier, J.F.L.; Kunz, K.; Roche, S.; Hedelius, J.; Neufeld, G.; Springett, S.; et al. TCCON Data from East Trout Lake, Canada, Release GGG2020R0. In *TCCON Data Archive*; CaltechDATA, California Institute of Technology: Pasadena, CA, USA, 2020. [[CrossRef](#)]

64. Strong, K.; Roche, S.; Franklin, J.E.; Mendonca, J.; Lutsch, E.; Weaver, D.; Fogal, P.F.; Drummond, J.R.; Batchelor, R.; Lindenmaier, R. TCCON data from Eureka, Canada, Release GGG2020R0. In *TCCON Data Archive*; CaltechDATA, California Institute of Technology: Pasadena, CA, USA, 2020. [[CrossRef](#)]
65. Sussmann, R.; Rettinger, M. TCCON data from Garmisch, Germany, Release GGG2020R0. In *TCCON Data Archive*; CaltechDATA, California Institute of Technology: Pasadena, CA, USA, 2020. [[CrossRef](#)]
66. Cheng, L.; Wang, W.; Sun, Y. TCCON data from Hefei, China, Release GGG2020R0. In *TCCON Data Archive*; CaltechDATA, California Institute of Technology: Pasadena, CA, USA, 2020. [[CrossRef](#)]
67. Blumenstock, T.; Hase, F.; Schneider, M.; Garca, O.E.; Sepulveda, E. TCCON Data from Izana, Tenerife, Spain, Release GGG2020R0. In *TCCON Data Archive*; CaltechDATA, California Institute of Technology: Pasadena, CA, USA, 2020.
68. Wennberg, P.O.; Roehl, C.; Blavier, J.F.; Wunch, D.; Landeros, J.; Allen, N. TCCON data from Jet Propulsion Laboratory, Pasadena, California, USA, Release GGG2020R0. In *TCCON Data Archive*; CaltechDATA, California Institute of Technology: Pasadena, CA, USA, 2020. [[CrossRef](#)]
69. Shiomi, K.; Kawakami, S.; Ohyama, H.; Arai, K.; Okumura, H.; Ikegami, H.; Usami, M. TCCON data from Saga, Japan, Release GGG2020R0. In *TCCON Data Archive*; CaltechDATA, California Institute of Technology: Pasadena, CA, USA, 2020. [[CrossRef](#)]
70. Hase, F.; Blumenstock, T.; Dohe, S.; Groß, J.; Kiel, M. TCCON data from Karlsruhe, Germany, Release GGG2020R1. In *TCCON Data Archive*; CaltechDATA, California Institute of Technology: Pasadena, CA, USA, 2020. [[CrossRef](#)]
71. Sherlock, V.; Connor, B.; Robinson, J.; Shiona, H.; Smale, D.; Pollard, D. TCCON data from Lauder, New Zealand, 125HR, Release GGG2020R0. In *TCCON Data Archive*; CaltechDATA, California Institute of Technology: Pasadena, CA, USA, 2020. [[CrossRef](#)]
72. Buschmann, M.; Petri, C.; Palm, M.; Warneke, T.; Notholt, J.; Engineers, A.S. TCCON data from Ny-Alesund, Svalbard, Norway, Release GGG2020R0. In *TCCON Data Archive*; CaltechDATA, California Institute of Technology: Pasadena, CA, USA, 2020. [[CrossRef](#)]
73. Wennberg, P.O.; Wunch, D.; Roehl, C.; Blavier, J.F.; Toon, G.C.; Allen, N.; Dowell, P.; Teske, K.; Martin, C.; Martin, J. TCCON data from Lamont, Oklahoma, USA, Release GGG2020R0. In *TCCON Data Archive*; CaltechDATA, California Institute of Technology: Pasadena, CA, USA, 2020. [[CrossRef](#)]
74. Warneke, T.; Messerschmidt, J.; Notholt, J.; Weinzierl, C.; Deutscher, N.; Petri, C.; Grupe, P.; Vuillemin, C.; Truong, F.; Schmidt, M.; et al. TCCON data from Orleans, France, Release GGG2020R0. In *TCCON Data Archive*; CaltechDATA, California Institute of Technology: Pasadena, CA, USA, 2020. [[CrossRef](#)]
75. Wennberg, P.O.; Roehl, C.; Wunch, D.; Toon, G.C.; Blavier, J.F.; Washenfelder, R.; Keppel-Aleks, G.; Allen, N.; Ayers, J. TCCON data from Park Falls, Wisconsin, USA, Release GGG2020R1. In *TCCON Data Archive*; CaltechDATA, California Institute of Technology: Pasadena, CA, USA, 2020.
76. Te, Y.; Jeseck, P.; Janssen, C. TCCON data from Paris, France, Release GGG2020R0. In *TCCON Data Archive*; CaltechDATA, California Institute of Technology: Pasadena, CA, USA, 2020. [[CrossRef](#)]
77. De Mazière, M.; Sha, M.K.; Desmet, F.; Hermans, C.; Scolas, F.; Kumps, N.; Zhou, M.; Metzger, J.M.; Dufлот, V.; Cammas, J.P. TCCON data from Reunion Island (La Reunion), France, Release GGG2020R0. In *TCCON Data Archive*; CaltechDATA, California Institute of Technology: Pasadena, CA, USA, 2020. [[CrossRef](#)]
78. Morino, I.; Ohyama, H.; Hori, A.; Ikegami, H. TCCON data from Rikubetsu, Hokkaido, Japan, Release GGG2020R0. In *TCCON Data Archive*; CaltechDATA, California Institute of Technology: Pasadena, CA, USA, 2020. [[CrossRef](#)]
79. Kivi, R.; Heikkinen, P.; Kyro, E. TCCON data from Sodankyla, Finland, Release GGG2020R0. In *TCCON Data Archive*; CaltechDATA, California Institute of Technology: Pasadena, CA, USA, 2020. [[CrossRef](#)]
80. Morino, I.; Ohyama, H.; Hori, A.; Ikegami, H. TCCON Data from Tsukuba, Ibaraki, Japan, 125HR, Release GGG2020R0. In *TCCON Data Archive*; CaltechDATA, California Institute of Technology: Pasadena, CA, USA, 2020. [[CrossRef](#)]
81. Deutscher, N.M.; Griffith, D.W.T.; Paton-Walsh, C.; Jones, N.B.; Velazco, V.A. TCCON data from Wollongong (AU), Release GGG2020R0. In *TCCON Data Archive*; CaltechDATA, California Institute of Technology: Pasadena, CA, USA, 2020. [[CrossRef](#)]
82. Sussmann, R.; Rettinger, M. TCCON data from Zugspitze, Germany, Release GGG2020R0. In *TCCON Data Archive*; CaltechDATA, California Institute of Technology: Pasadena, CA, USA, 2020.
83. Zhong, J.; Zhang, X.; Guo, L.; Wang, D.; Miao, C.; Zhang, X. Ongoing CO₂ monitoring verify CO₂ emissions and sinks in China during 2018–2021. *Sci. Bull.* **2023**, *in press*. [[CrossRef](#)]
84. Kataoka, F.; Crisp, D.; Taylor, T.; O'Dell, C.; Kuze, A.; Shiomi, K.; Suto, H.; Bruegge, C.; Schwandner, F.; Rosenberg, R.; et al. The Cross-Calibration of Spectral Radiances and Cross-Validation of CO₂ Estimates from GOSAT and OCO-2. *Remote Sens.* **2017**, *9*, 1158. [[CrossRef](#)]
85. Wunch, D.; Wennberg, P.O.; Osterman, G.; Fisher, B.; Naylor, B.; Roehl, C.M.; O'Dell, C.; Mandrake, L.; Viatte, C.; Kiel, M.; et al. Comparisons of the Orbiting Carbon Observatory-2 (OCO-2) X-CO₂ measurements with TCCON. *Atmos. Meas. Tech.* **2017**, *10*, 2209–2238. [[CrossRef](#)]
86. Bao, Z.; Zhang, X.; Yue, T.; Zhang, L.; Wang, Z.; Jiao, Y.; Bai, W.; Meng, X. Retrieval and Validation of XCO₂ from TanSat Target Mode Observations in Beijing. *Remote Sens.* **2020**, *12*, 3063. [[CrossRef](#)]

Disclaimer/Publisher's Note: The statements, opinions and data contained in all publications are solely those of the individual author(s) and contributor(s) and not of MDPI and/or the editor(s). MDPI and/or the editor(s) disclaim responsibility for any injury to people or property resulting from any ideas, methods, instructions or products referred to in the content.